Chiral and Achiral Crystal Structures of $Au_{25}(PET)_{18}^{0}$ Reveal Effects of Ligand Rotational Isomerization on Optoelectronic Properties

Dr. Gowri Udayangani Kuda-Singappulige[† § ‡], Dr. Phillip S. Window[‡ #], Dr. Christopher A. Hosier[¶ #], Dr. Ian D. Anderson[#], Prof. Dr. Christine M. Aikens[§], and Prof. Dr. Christopher J. Ackerson[#*]

[#]Department of Chemistry, Colorado State University

[§]Department of Chemistry, Kansas State University

ABSTRACT: The crystal structures of 4 ligand-rotational isomers of $Au_{25}(PET)_{18}$ are presented. Two new ligand-rotational isomers are revealed, and two higher-quality structures (allowing complete solution of the ligand shell) of previously solved $Au_{25}(PET)_{18}$ clusters are also presented. One of the structures lacks an inversion center, making it the first chiral $Au_{25}(SR)_{18}$ structure solved. These structures combined with previously published $Au_{25}(SR)_{18}$ structures enable an analysis of the empirical ligand conformation landscape for $Au_{25}(SR)_{18}$ clusters. This analysis shows that the dihedral angles within the PET ligand are restricted to certain observable values, and also that the dihedral angle values are interdependent, in a manner reminiscent of biomolecule dihedral angles such as those in proteins and DNA. The influence of ligand conformational isomerism on optical and electronic properties was calculated, revealing that the ligand conformations affect the nanocluster absorption spectrum, which potentially provides a way to distinguish between isomers at low temperature

$Au_{25}(SR)_{18}$ is the benchmark cluster for gold-thiolate monolayer protected clusters (MPCs).[1] Due to its facile synthesis and robust ambient stability, it is the best studied MPC, which includes compounds such as $Au_{38}(SR)_{24}$, $Au_{102}(SR)_{44}$, $Au_{144}(SR)_{60}$, $Au_{279}(SR)_{84}$ and $Au_{333}(SR)_{79}$, among others.[2–6] Findings made first on $Au_{25}(SR)_{18}$ that presaged similar findings across the series of clusters include redox dependent paramagnetism,[7–11] interparticle exchange of ligands,[12] interparticle exchange of metals,[12] and electrocatalysis.[13] $Au_{25}(SR)_{18}$ was the first MPC that was predicted correctly in terms of structure prior to knowledge of the X-ray structure.[14]

The optical, electronic and magnetic properties of $Au_{25}(SR)_{18}$ depend upon the ligand shell. Indeed, the optical and electronic properties of the cluster are notably sensitive to ligand identity and solvation.[15] [16] [17] [18][19–21][22] The relationship between ligand shell isomers and optical / electronic properties is presently obscure.

For structural studies, the SR group used most commonly is phenylethanethiolate (PET). $Au_{25}(PET)_{18}$ has been crystallographically determined in 3 oxidation states.[23–25] [26] The crystal structures show a 13-gold atom filled-icosahedral core, with the remaining 12 gold atoms incorporated into each of 6 SR-Au(I)-SR-Au(I)-SR units that are described as "semi-rings" due to their property of forming a semi-circle around the Au_{13} icosahedron. Figure 1, showing new ligand conformations determined in this work, also depicts the inorganic framework observed in all so-far solved structures of $Au_{25}(SR)_{18}$.

The PET ligands used in these crystal structures can accommodate many rotational isomers. Each PET ligand contains 3 rotatable bonds, specifically the S-C, C-C, and C-Ph bonds. Considering 18 ligands per cluster with 3 rotating bonds per ligand results in an enormous conformational space. Jiang calculated the ligand conformational energy landscapes for 46,656 conformations of $Au_{25}(SR)_{18}$.[27] This analysis found several global minima for ligand rotational isomer sets, including some that were of lower energy than known crystal structures. Notably this conformational space exploration omits consideration of π-interactions among phenyl containing ligands. Inclusion of π-interactions may substantially restrict the number of ambiently observable ligand configurations. More recently, some topological isomers of lower energy have been predicted computationally[28] and confirmed experimentally[29] in the gas phase.

Several papers have highlighted ligand-ligand interactions that extend large distances over the surface of MPCs, somewhat reminiscent of the long-range secondary-structure interactions well-known in proteins.[3] Accordingly, an NMR study of the ligand orientations in $Au_{102}(SR)_{44}$ suggests that ligands are indeed substantially restrained in their functional movement.[30] In that study, 19 of the 22 symmetry-independent structures appeared to be in the same orientation in solution as they were in the crystal structure, despite the possibility for rotation around the S-Ph bond. Here π-interaction networks appear to restrict the movement of ligands. While $Au_{102}(SR)_{44}$ may be relatively similar in ligand configuration in solid-state and solution, infrared spectroscopy suggests that the $Au_{38}(PET)_{24}$ cluster shows markedly different ligand rotational configurations in solution and solid-state.[31]

Herein we present 4 crystal structures of $Au_{25}(PET)_{18}^{0}$. Two of these structures show previously unobserved ligand and rotational isomers of $Au_{25}(PET)_{18}^{0}$. Two of the structures are higher quality replicas of previously solved isomers.[24,25] One of the new crystal structures is remarkable in that it is chiral (the first structure of $Au_{25}(SR)_{18}$ to lack an inversion center). The electronic properties of each of these structures were calculated, revealing the nature and extent of ligand isomer influence on $Au_{25}(SR)_{18}$ electronic properties.

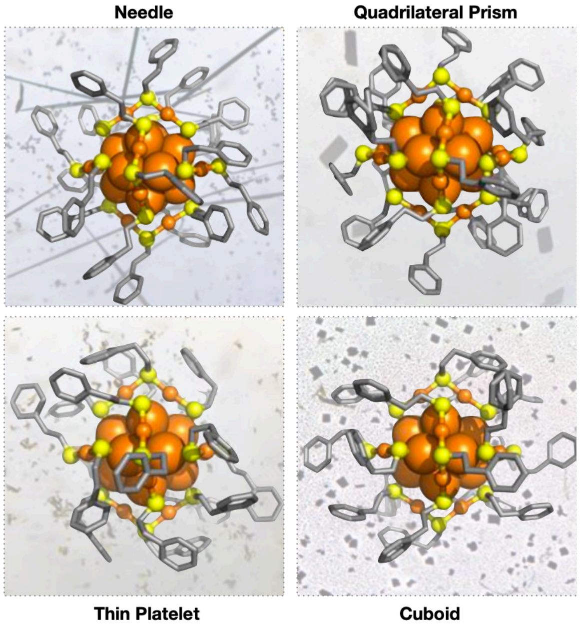

Figure 1. Four ligand shell isomorphs of $Au_{25}(PET)_{18}$ are shown. The different isomorphs are observed in each of 4 distinct crystal habits. Images of the crystals producing each crystal structure are shown behind each crystal structure. Gold atoms are rendered in orange, sulfur in yellow and carbon in grey.

$Au_{25}(PET)^{0}$ Crystal Structure Determination

$Au_{25}(PET)_{18}^{0}$ crystals were obtained by oxidizing $Au_{25}(PET)_{18}^{-1}$ during crystallization. Different crystallization methods resulted in four different habits of $Au_{25}(PET)_{18}^{0}$ crystals (Figure S2-S5). Single crystal x-ray diffraction data was collected using a XtaLAB Synergy Custom FR-X MM007HF diffractometer. Full details about crystallization and data collection can be found in the supporting information. Structures were solved in Olex2 using SHELXL for refinement.

Figure 1 shows each of the four structures. The structures are named according to their crystal habit. The thin platelet and needle crystal habits produced new crystal structures revealing previously unobserved ligand orientations for $Au_{25}(PET)_{18}^{0}$. The cuboid and quadrilateral prism are replicas of previously published crystal structures.

In the case of the quadrilateral prism, the structure reported here represents an improvement of the prior crystal structure. The prior crystal structure[25] was incompletely determined in the ligand shell. The quadrilateral prism crystal structure presented herein completely determines the ligand shell. As judged by crystallographic correlation of data to model statistics, R_1 improved from 0.0516 in the prior structure to 0.025 in the current structure. Similarly, Goodness of Fit (GooF) improved from 1.243 to 1.025. This improved crystal structure allows much higher confidence in the assignment of ligand positions.

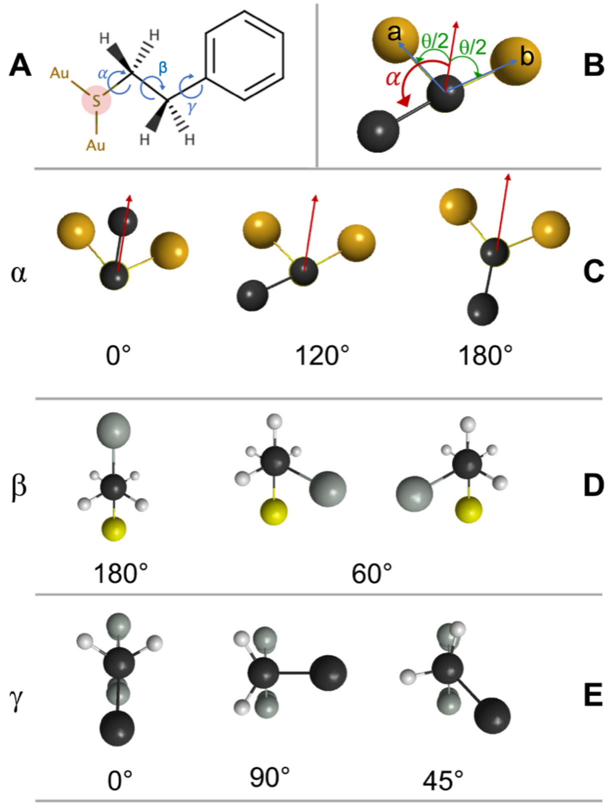

Figure 2. Panel A shows the rotatable bonds α, β, and γ in phenylethanethiolate bonded to 2 gold atoms. Panel B shows the definition of the α angle with respect to the bisector of the Au-S-Au angle. Panels C, D, and E show Newman projections of the α, β, and γ angles at representative rotations. For β, the 60º angles are gauche and the 180º angle is anti. For γ, the Ph group is shown pointed away from the viewer and the alpha C of the ethyl group faces the viewer. Key: Gold; Au, Yellow; S, Black; C in ethyl group, Gray: C in phenyl group, White: H.

The different crystal structures arose from different crystallization conditions. The Needle crystals were made by addition of ethanol to a saturated solution of $Au_{25}(PET)_{18}^{0}$ in toluene and took over a month to form. The quadrilateral prism crystals were grown by layering ethanol on top of a concentrated solution of $Au_{25}(PET)_{18}^{0}$, and crystals were observed within 3 days. The thin-platelet crystals were grown from Au25(PET)180 dissolved in acetonitrile, with 0.1% tetramethylsilane present. Crystals were apparent within a day. The cuboid crystals were formed with Au25(PET)18-1 in toluene, with tetra-n-octylammonium bromide present and ethanol added until the solution appeared cloudy. Crystals could be observed within 30 minutes. We cannot explain why these different crystallization conditions resulted in different structures.

The crystal structure arising from the needle habit stands out from all other crystal structures of $\mathrm{Au}_{25}(\mathrm{PET})_{18}$ in that it is chiral. All other $\mathrm{Au}_{25}(\mathrm{PET})_{18}$ structures to-date incorporate an inversion center. However, it has been known for decades that incorporation of chiral ligands results in chiral clusters for $\mathrm{Au}_{25}(\mathrm{PET})_{18}$.[32]

These four new crystal structures, combined with 5 prior crystal structures, enables an examination of the empirical ligand conformation space. Higher quality crystal structures enable this analysis, as the ligands are often incompletely determined in lower quality crystal structures.

Analysis of observed PET ligand bond rotations.

The ligands of $\mathrm{Au}_{25}(\mathrm{PET})_{18}^{0}$ sit within each of 6 semi-rings. Each semi-ring contains 3 ligands, separated by Au(I) atoms. Thus, each ligand is anchored in an SR-Au(I)-SR-Au(I)-SR bonding environment. Within the semi-ring, the ligands can be cis-cis, cis-trans, or trans-trans relative to each other. Figure S1 shows the possible cis/trans arrangements and describes the ligand relationships to each other within semi-rings.

Each PET ligand contains 3 bonds around which rotation can occur—these are the S-C, the C-C and the C-Ph bonds. Previous analyses[27] of PET ligand rotational space described ligand rotamers as staggered, eclipsed, anti- and / or gauche. Instead, our analysis defines three rotatable bonds for the gold-cluster anchored phenylethanethiol (Figure 2). Each bond has a definable angle, also shown in Figure 2. These angles – α, β, and γ – describe the configuration of each of the 3 bonds around which rotation may occur in PET ligands.

The *α* angle is the dihedral angle of the S-C bond within the PET ligand (Figure 2, panel B). Because the S atom is bonded to two Au atoms, but also maintains a tetrahedral geometry, the dihedral angle is defined as shown in Figure 2B. Briefly, when viewed along the S-C bond, angle *α* is measured as the dihedral angle between the C-C bond and the bisector of the Au-S-Au angle. Newman projections showing orientations corresponding to *α* values of 0, 60 and 120 are shown in Figure 2C. Note that α does not distinguish between edge and middle ligands on the S-Au-S-Au-S staple motif. The *β* angle is defined as the S-C-C-C dihedral angle (e.g., corresponding to rotation around the ethyl bond), as illustrated in Figure 2A. *β* here is conventionally defined and incorporates anti (180°) and gauche (60°) staggered configurations, and would also account for eclipsed configurations (0°, 120°). We do not distinguish between 60° and -60° gauche structures in this work. Figure 2D shows Newman projections of these bond rotations.

The *γ* angle is the dihedral angle of the C-Ph bond – specifically the rotation angle of the Ph group relative to the ethyl group. Figure 2E shows a Newman projection defining this rotation angle. At angles larger than 90°, the opposite side of the Ph group begins approaching the CH_2 group.

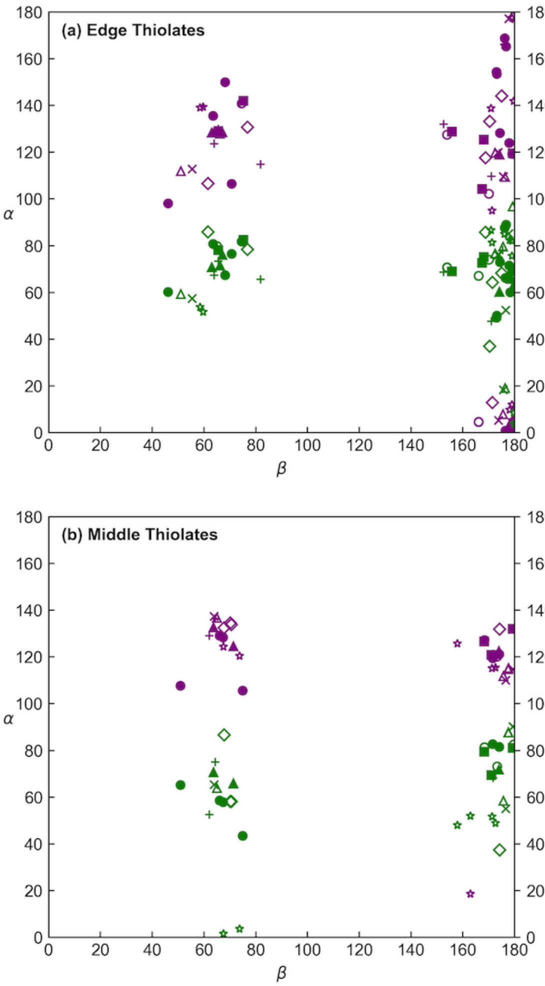

Figure 3. A scatter plot showing α, β, and γ angles for PET ligands in all reported $\mathrm{Au}_{25}(\mathrm{PET})_{18}$ isomers. Purple points represent correlations of α and β angles; green points represent correlations of β and γ angles. From the current structures, (+) is the thin platelet crystal habit, (×) the quadrilateral prism, (∗) the needle, and to the cuboid. From prior published structures, filled squares are from reference 24, open circles from reference 23, closed circles from reference 26, and triangles (open and closed) from reference 25. Two data points overlap at each point arising from centrosymmetry for all crystal structures except for the needle isomer due to its lower symmetry.

Because the opposite sides of the Ph group are symmetrically indistinguishable, *γ* values range from 0° to 90°.

An analysis of all 9 available crystal structures[23–26] (representing 90 symmetry unique ligands) shows each bond dihedral angle has a set of ‘preferred’ values. Figure 3 shows a scatter plot of α, β, and γ values.

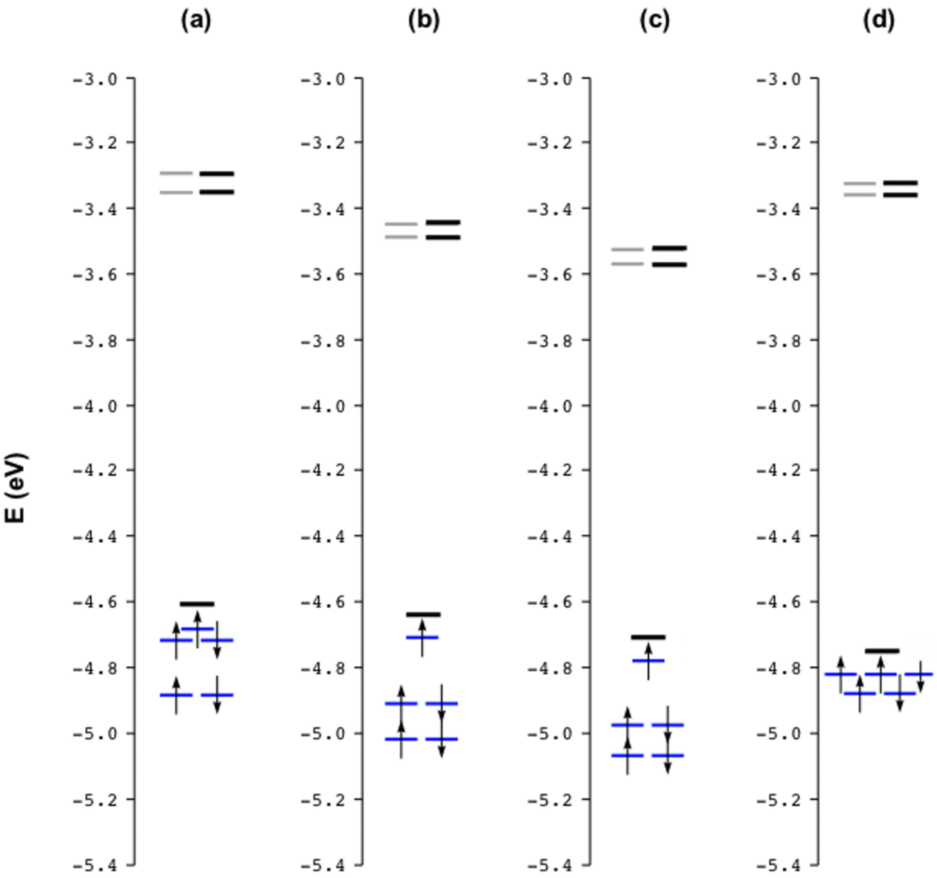

Figure 4. Orbital energy level diagrams of the crystal structures (0 charge state) of (a) thin platelet, (b) quadrilateral prism, (c) needle and (d) cuboid. The virtual orbital energy levels in gray and black represent α and β spin orbitals respectively.

From this plot, it is clear that α angles (purple points) group around 120° and 0°, with more at 120°. No α values between 25 and 85 are observed in the current data set.

The *β* angle values (shown in both green and purple data) group around 60° and 180°, which are anti- and gauche-staggered orientations. β angles between 0º and 40º as well as 85º to 145º are not observed. Of note, no eclipsed (0° or 120°) orientations are observed.

The *γ* angle values (green points) group around 80º; however, essentially all possible values of γ in the range of 0° to 90° are observed in the overall dataset, so the preferences of the γ angle for any given angle is not as strong as it is for α and β. This suggests freer rotation around the *γ* angle.

The analysis of Figure 3 shows clearly that the dihedral angles α, β, and γ are interdependent. When β is in a gauche-configuration (66°±7°), the angles of α and γ are notably restricted. The α angle in particular falls in a very narrow range of 127º±11º. The γ angle is somewhat less restricted with an average angle and standard deviation of 67º±16º.

When β is in an anti- configuration (173°±6°) the observed angles of α and γ are more promiscuous; α angles are observed in two groups – one at 5°±5° and a second at 127°±19°. When β is in an anti- configuration, many angles of γ are observable (67°±18°).

Considering the middle versus edge positions of ligands in the semi-ring, the α/β angles do not appear notably different. However, the edge position appears to allow more conformational flexibility in the β/γ angle interdependence.

Overall, Figure 3 shows the observable conformational landscape of ligands in the well-studied cluster $Au_{25}(PET)_{18}$. In a manner that is akin to many other complex molecules – such as proteins, DNA, and sugars – dihedral angles appear to be restricted and interdependent. In this sense, Figure 3 can be viewed as a “Ramachandran-like-plot” for PET ligands on $Au_{25}(PET)_{18}$.

Computational analysis of electronic properties of $Au_{25}(PET)_{18}^0$ isomers

The four structures reported in this paper prompted a computational analysis of how electronic properties of the cluster might change as a function of ligand rotational isomorphism. All four systems have an unpaired electron, so the alpha and beta electrons are treated in an unrestricted fashion. We observe that in these four isomers, the HOMO-LUMO (H-L) gaps in α-spin orbitals and β-spin orbitals are anticorrelated (Figure 4). This inverse behavior originates from the splitting of the 1P superatomic orbitals. All three 1P α-spin orbitals are occupied whereas only two 1P β-

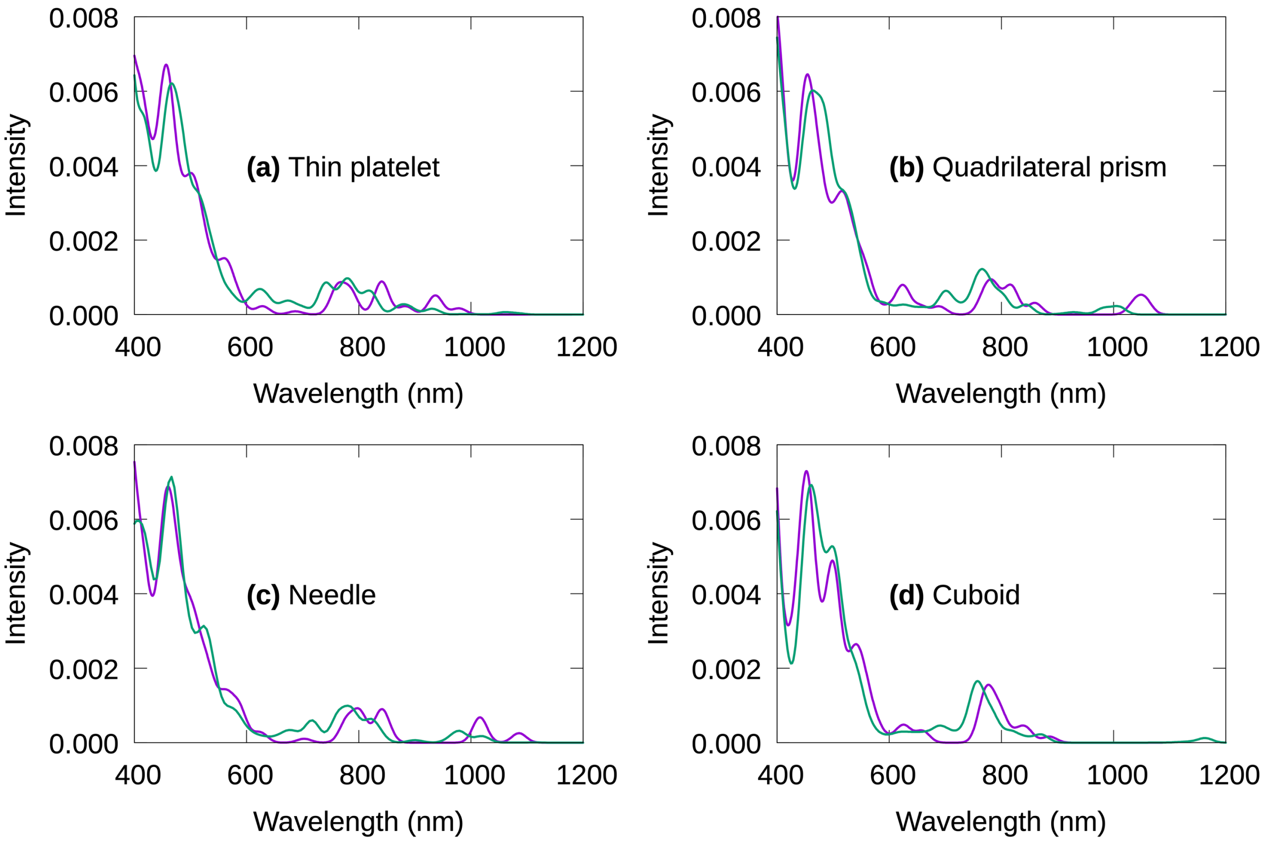

Figure 5. Calculated absorption spectra. Green: charge = 0; Purple: charge = -1.

spin orbitals are occupied. The α-spin H-L gap is the energy between the 1P and 1D superatomic orbitals whereas the β-spin H-L gap comes from the difference between the two highest energy 1P orbitals. A greater splitting of the 1P orbitals leads to a smaller α-spin H-L gap (because the highest occupied 1P becomes closer in energy to the unoccupied 1D) and a larger β-spin H-L gap (due to the increased splitting of the 1P orbitals) and vice versa. The maximum splitting occurs in the quadrilateral prism (QLP) and needle structures. Therefore, the QLP and the needle have the lowest H-L gap in α-spin orbitals and the highest β-spin H-L gap among the four isomers (Table 1). The thin platelet has the next highest splitting followed by the cuboid with the least splitting. This explains the overall α-spin H-L gap order of Needle < QLP < Thin platelet < Cuboid and β-spin H-L gap order of Needle > QLP > Thin platelet > Cuboid.

The H-L gap indicates that the QLP and the needle structure have similar electronic structure which is different from the thin platelet and the cuboid structures. The QLP and the needle have the lowest H-L gap for the α-spin orbitals and the highest H-L gap in β-spin orbitals among the four isomers. The similarity between the QLP and the needle isomers can be attributed to the similarities in their structures. The main similarity is that both isomers have the same number of anti and gauche conformations (each contains 14 anti and 4 gauche conformations) around the CH$_2$-CH$_2$ bond in the PET ligands (β dihedral angle, Table 2). Considering the rotations around S-CH$_2$ in the PET ligands (α angles), both QLP and needle have a more widely spread distribution (α angles around 0°, 120° and 180°) than the thin platelet and the cuboid isomers. The α dihedral angles in the thin platelet and cuboid are mostly centered around 120°; 16 ligands occur around 120° and only two ligands have α closer to 0°. In contrast, the QLP and needle isomers respectively have 4 and 6 ligands with α near 0°. QLP and needle also have two ligands with α close to 180°, while no such orientations were observed in thin platelet and cuboid. The QLP and needle isomers have ligands with very small γ angles (<20°), whereas thin platelet and cuboid possess ligands with large γ angles. Even though the QLP structure contains a center of inversion and the needle does not, the similarities in the distributions of α and β dihedrals in the two isomers lead to similarities in the electronic structure.

Both cuboid and the thin platelet have the same distribution of α angles around S-CH$_2$ as discussed earlier (16 ligands with α around 120° and 2 ligands with α closer to 0°). The number of PET ligands with anti and gauche orientation around the CH$_2$-CH$_2$ bond (β) in the cuboid structure is 10 and 8 respectively (Table 2), while that in the thin platelet is 8 and 10 respectively. The distribution of γ angles is more spread out in cuboid, whereas all 18 ligands in thin platelet have γ angles between 45º and 80º. The cuboid, which has 10 anti orientations and more flexible phenyl rotations, has the smallest splitting of the 1P orbitals leading to larger alpha-spin H-L gap (smaller beta-spin

H-L gap). In contrast, 1P splitting of the thin platelet with 8 anti orientations and less flexible phenyl rotations, is larger than in the cuboid, resulting a smaller alpha-spin (larger beta-spin) H-L gap.

The absorption spectra (green: charge = 0) of QLP and the needle show a peak around 1000 nm, followed by a stronger peak around 800 nm (Figure 5). In contrast, the lowest energy peak in the thin platelet arises around 900 nm followed by a stronger, broader peak around 800 nm. In the cuboid structure, a weak peak is observed at around 1200 nm. However, a stronger peak arises around 800 nm. The lower energy (near-IR) portion of the spectra clearly reflects the differences in the electronic structure originating from the structural distortions. This suggests that at low temperature the experimental spectra could be able to distinguish between the isomers that differ from each other by different rotations of the PET ligands. However, in the 400-800 nm region, all isomers show peaks around 470, 520, and 780 nm. Therefore, the spectral properties in the UV/Vis region are expected to be similar in these different isomers.

We also compared the difference in the absorption spectra of nanoparticles with charge states 0 (green) and -1 (purple) (Figure 5). The closed-shell calculations for the anion yields similar spectra as the open-shell calculations for the neutral charge, which is the experimentally observed charge state in this work. The shapes of the spectra are retained when the charge is changed to -1. The only difference we observed was a slight redshift of the low-energy excitations when going from neutral to the anionic charge state.

	Thin Platelet	Quad. Prism	Needle	Cuboid
Anti-	8	14	14	10
Gauche-	10	4	4	8
Cis-Cis	0	0	0	0
Cis-Trans	0	0	0	0
Trans-Trans	6	6	6	6
Symmetric	Yes	Yes	No	Yes

Table 2. Geometric characteristics of 4 $Au_{25}(PET)_{18}$ crystal structures.

All 27 components of the static second order hyperpolarizability tensor of the three centrosymmetric isomers are zero; for the needle isomer, these components are nonzero, leading to a non-zero βvec as expected. The needle isomer exhibits a βvec value of 3.005×10^{-30} esu at the BP86/DZ level of theory, which is similar to the experimentally observed βHRS,0 of 5 (±1) × 10-30 esu in [Au25(captopril)18]-1,[33] a non-centrosymmetric nanoparticle due to the chiral captopril ligands.

It must be noted that single point energies on individual structures do not account for packing effects, and thus single point energies on isolated structures do not necessarily provide information about the most favorable isomers in the crystal.

	HOMO-LUMO (eV)	
Isomer Identity	**α**	**β**
Thin Platelet	1.297	0.110
Quadrilateral prism	1.189	0.268
Needle	1.188	0.269
Cuboid	1.448	0.067

Table 1. HOMO-LUMO gap of the crystal structures (neutral charge state)

Experimental

Materials and Methods

Gold (III) chloride trihydrate (Sigma-Aldrich, ACS reagent, ≥49.0% Au basis), tetra-*n*-octylammonium (TOA) bromide (Acros Organics, 98% purity), sodium borohydride (Sigma-Aldrich, ≥99% purity), 2-phenylethanethiol (PET, Sigma-Aldrich, ≥99% purity), tetrahydrofuran (Fisher Scientific, certified, stabilized with 0.025% butylated hydroxytoluene), methanol (Fisher Scientific, certified ACS, 99.9% assay), ethanol (Fisher Scientific, 200 proof), toluene (Sigma-Aldrich, ≥99.5% purity), acetonitrile-D3 (Cambridge Isotope Laboratories, 99.8% D), and *trans*-2-[3-(4-*tert*-butylphenyl)-2-methyl-2-propenylidene] malonitrile (Sigma-Aldrich, ≥99.0% [HPLC]) were all used without further purification. Water was obtained using a Thermo Scientific Barnstead Nanopure set to 18.2 MΩ·cm.

Synthesis of $[TOA][Au_{25}(PET)_{18}]$

This procedure was adapted from a previously published report. To a 300 mL roundbottom flask containing 140 mL tetrahydrofuran was added 2.0 g $HAuCl_4 \cdot 3H_2O$ and 3.12 g tetra-*n*-octylammonium bromide, which was allowed to stir for 30 minutes until a dark orange color was observed. 3.6 mL of 2-phenylethanethiol was then added, and the resulting solution was stirred overnight (15-18 hours). A separate fresh solution containing 1.94 g sodium borohydride in 48 mL H_2O was produced in a 125 mL Erlenmeyer flask and cooled to 0 °C prior to adding it to the gold-containing solution in a single continuous stream. The combined solutions were then stirred for 48 hours, followed by separation and evaporation of the organic layer. This afforded a brown oil which was re-dissolved in several milliliters of dichloromethane and separated into four 50 mL conical vials. The conical vials were filled with methanol and placed in a centrifuge at 4000 rpm for 30 minutes. The supernatant was decanted and the precipitate was washed twice more by addition of methanol and centrifugation. Extraction with dichloromethane and subsequent evaporation of the solvent afforded the final product.

Crystallization of Cuboid $Au_{25}(PET)_{18}^0$

$[TOA][Au_{25}(PET)_{18}]$ was dissolved in a minimal amount of toluene. To this solution was added tetra-*n*-octylammonium bromide in a 1:1 mass ratio to the cluster. Ethanol was added and mixed until the solution appeared slightly cloudy, after which the solution was centrifuged. The resulting supernatant was heated slightly on a hot plate at the lowest setting. During this time, the cluster oxidized. Cuboid crystals could be observed between 30 minutes and one week depending on the exact ratio of toluene and ethanol.

Crystallization of Quadrilateral Prism $Au_{25}(PET)_{18}^0$
Cuboid crystals of $Au_{25}(PET)_{18}^0$ were dissolved in a minimal solution of toluene. Ethanol was gently layered on top of the solution in an approximate 1:1 volume ratio and allowed to slowly diffuse at room temperature. Prism crystals were observed within three days.

Crystallization of Thin Platelet $Au_{25}(PET)_{18}^0$
Cuboid crystals of $Au_{25}(PET)_{18}^0$ were dissolved in a minimal amount of deuterated acetonitrile in an NMR tube. To this solution, tetramethylsilane was added in a 1:1000 volume ratio to deuterated acetonitrile. Thin platelet crystals were observed within one day.

Crystallization of Needle $Au_{25}(PET)_{18}^0$
Amorphous $Au_{25}(PET)_{18}$ powder (oxidized through extensive air drying) was dissolved in a minimal amount of toluene. Ethanol was added and mixed until the solution appear slightly cloudy. Crystals could be observed after approximately one month.

Single Crystal X-ray Diffraction Data Collection
Diffraction experiments were performed using a XtaLAB Synergy Custom FR-X diffractometer set to a generator level of 1200 W (40 kV and 30 mA) and a Pilatus P200K 3R detector. Data was collected to a resolution of 0.84 Å using a copper irradiation source (1.54184 Å) with an exposure time of 0.5 seconds and detector distance of 28 mm. Initial processing of the raw diffraction data was done using CrysAlis (Pro). Numerical and analytical absorption corrections were attempted but not utilized in the final structures as they did not improve statistical values. SHELXT and SHELXL were used in determination of the nanocluster structures through a full-matrix least-squared against F^2 approach.

Conclusions

Four new crystal structures of $Au_{25}(PET)_{18}$ representing 2 previously unobserved rotational isomers and 2 additional higher quality structures of previously observed rotational isomers are determined. These 4 structures, as well as 5 prior crystal structures of $Au_{25}(SR)_{18}$, allow an analysis of the ligand rotational space for this well-studied cluster. Additional electronic analysis of the 4 new $Au_{25}(SR)_{18}$ clusters reveals notable differences in their spectra. The same spectral shape is observed for the two charge states with a slight redshift of the negatively charged species at low energy range. The distinct spectral features of the four isomers suggests that the experimental spectra could distinguish the four isomers, at least at low temperature, although the isomers differ from each other only by different rotations within PET ligands. Notably, one of the newly-observed isomers is chiral. Its second order hyperpolarizability is predicted to be similar to other Au_{25} nanoparticles that incorporate chiral ligands, which suggests that this presents a unique approach to producing nonlinear crystals.

ASSOCIATED CONTENT

Supporting Information

Images of crystals and schematics of ligand orientations are available as supporting information.

Deposition Number(s) <url href="https://www.ccdc.cam.ac.uk/services/structures?id=doi:10.1002/chem.202202780"> 2164642 (for the thin platelet crystal), 2164641 (for the quadrilateral prism crystal), 2164640 (for the cuboid crystal), 2164639 (for the needle crystal), </url> contain(s) the supplementary crystallographic data for this paper. These data are provided free of charge by the joint Cambridge Crystallographic Data Centre and Fachinformationszentrum Karlsruhe <url href="http://www.ccdc.cam.ac.uk/structures">Access Structures service</url>.

AUTHOR INFORMATION

Corresponding Author

* C.J. Ackerson, ackerson@colostate.edu
http://ackerson.colostate.edu

Present Addresses

† Present Address for G.U.K.-S: Department of Chemical and Biological Engineering, Illinois Institute of Technology

¶ Present Address for C.A.H.: Unilever Food Innovation Centre – Hive bronland 14, 6708WH Wageningen, Netherlands

Author Contributions

The manuscript was written through contributions of all authors. All authors have given approval to the final version of the manuscript. ‡These authors contributed equally.

Funding Sources

P.S.W., C.A.H., I.D.A. and C.J.A. were supported by the National Science Foundation (CHE-1905179, CHE-2204110) of the United States.

G.U.K.-S. and C.M.A. were supported by the National Science Foundation (CHE-1905048) of the United States. The computing for this work was performed on the Beocat Research Cluster at Kansas State University, which is funded in part by NSF grants CHE-1726332, CNS-1006860, EPS-1006860, and EPS-0919443.

TOC Graphic:

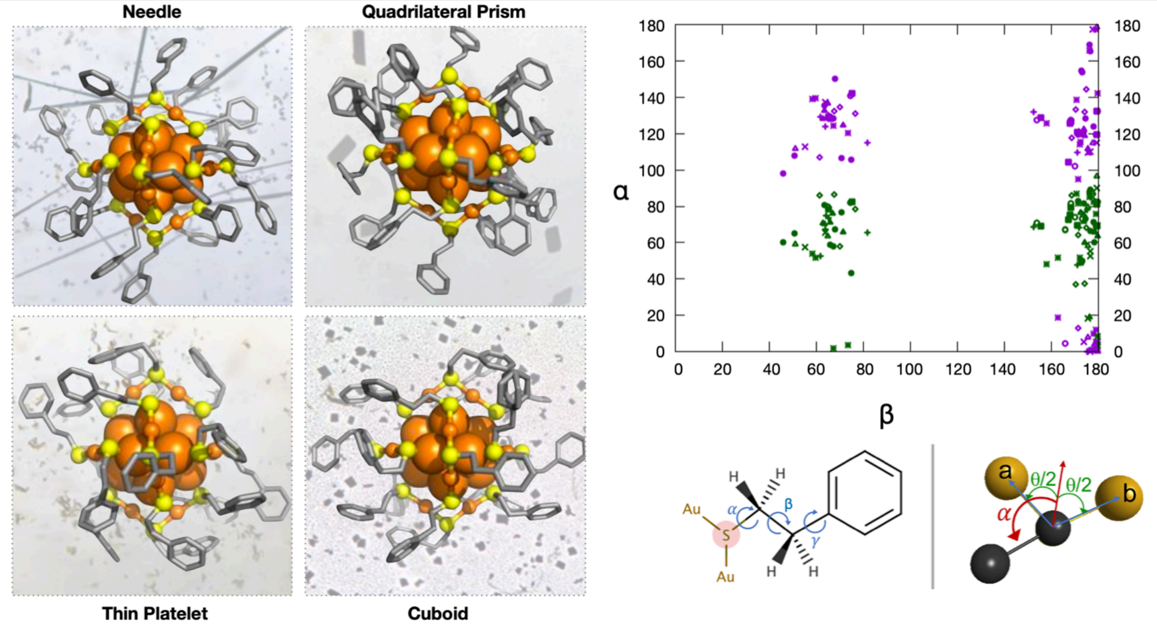

Analysis of all Au_{25}(phenylethanethiol)$_{18}$ crystal structures, including 2 novel clusters, reveals that ligand rotational angles are interdependent and constrained to a narrow range of values.

Twitter Handles

CJA: @d0cack

CJA Lab: @AckersonLab

CSU Chemistry: @csu_chemistry

REFERENCES

[1] J. F. Parker, C. A. Fields-Zinna, R. W. Murray, *Accounts Chem Res* **2010**, *43*, 1289–1296.

[2] H. Qian, W. T. Eckenhoff, Y. Zhu, T. Pintauer, R. Jin, *J Am Chem Soc* **2010**, *132*, 8280 8281.

[3] P. D. Jadzinsky, G. Calero, C. J. Ackerson, D. A. Bushnell, R. D. Kornberg, *Science* **2007**, *318*, 430 433.

[4] T. G. Schaaff, M. N. Shafigullin, J. T. Khoury, I. Vezmar, R. L. Whetten, *J Phys Chem B* **2001**, *105*, 8785–8796.

[5] N. A. Sakthivel, A. Dass, *Accounts Chem Res* **2018**, *51*, 1774–1783.

[6] H. Qian, Y. Zhu, R. Jin, *Proc National Acad Sci* **2012**, *109*, 696–700.

[7] M. Zhu, C. M. Aikens, M. P. Hendrich, R. Gupta, H. Qian, G. C. Schatz, R. Jin, *J Am Chem Soc* **2009**, *131*, 2490 2492.

[8] A. Venzo, S. Antonello, J. A. Gascón, I. Guryanov, R. D. Leapman, N. V. Perera, A. Sousa, M. Zamuner, A. Zanella, F. Maran, *Anal Chem* **2011**, *83*, 6355 6362.

[9] R. S. McCoy, S. Choi, G. Collins, B. J. Ackerson, C. J. Ackerson, *Acs Nano* **2013**, *7*, 2610 2616.

[10] C. Zeng, A. Weitz, G. Withers, T. Higaki, S. Zhao, Y. Chen, R. R. Gil, M. Hendrich, R. Jin, *Chem Sci* **2019**, DOI 10.1039/c9sc02736j.

[11] P. S. Window, C. J. Ackerson, *Inorg Chem* **2020**, *59*, 3509–3512.

[12] K. R. Krishnadas, A. Baksi, A. Ghosh, G. Natarajan, A. Som, T. Pradeep, *Accounts Chem Res* **2017**, *50*, 1988–1996.

[13] D. R. Kauffman, D. Alfonso, C. Matranga, H. Qian, R. Jin, *J Am Chem Soc* **2012**, *134*, 10237–10243.

[14] J. Akola, M. Walter, R. L. Whetten, H. Häkkinen, H. Grönbeck, *J Am Chem Soc* **2008**, *130*, 3756 3757.

[15] A. Tlahuice-Flores, R. L. Whetten, M. Jose-Yacaman, *J Phys Chem C* **2013**, *117*, 20867–20875.

[16] J. Akola, K. A. Kacprzak, O. Lopez-Acevedo, M. Walter, H. Grönbeck, H. Häkkinen, *J Phys Chem C* **2010**, *114*, 15986–15994.

[17] J. Jung, S. Kang, Y.-K. Han, *Nanoscale* **2012**, *4*, 4206–4210.

[18] T. Dainese, S. Antonello, J. A. Gascón, F. Pan, N. V. Perera, M. Ruzzi, A. Venzo, A. Zoleo, K. Rissanen, F. Maran, *Acs Nano* **2014**, *8*, 3904 3912.

[19] C. M. Aikens, *J Phys Chem Lett* **2010**, *1*, 2594 2599.

[20] C. M. Aikens, *J Phys Chem* **2009**, *113*, 10811 10817.

[21] R. D. Senanayake, C. M. Aikens, *Phys Chem Chem Phys Pccp* **2020**, *22*, 5272–5285.

[22] W. Kurashige, S. Yamazoe, M. Yamaguchi, K. Nishido, K. Nobusada, T. Tsukuda, Y. Negishi, *J Phys Chem Lett* **2014**, *5*, 2072–2076.

[23] M. W. Heaven, A. Dass, P. S. White, K. M. Holt, R. W. Murray, *J Am Chem Soc* **2008**, *130*, 3754–3755.

[24] M. A. Tofanelli, K. Salorinne, T. W. Ni, S. Malola, B. Newell, B. Phillips, H. Häkkinen, C. J. Ackerson, *Chem Sci* **2015**, *7*, 1882–1890.

[25] M. Zhu, W. T. Eckenhoff, T. Pintauer, R. Jin, *J Phys Chem C* **2008**, *112*, 14221 14224.

[26] M. Zhu, C. M. Aikens, F. J. Hollander, G. C. Schatz, R. Jin, *J Am Chem Soc* **2008**, *130*, 5883–5885.

[27] R. Ouyang, D. Jiang, *J Phys Chem C* **2015**, *119*, 21555–21560.

[28] M. F. Matus, S. Malola, E. K. Bonilla, B. M. Barngrover, C. M. Aikens, H. Häkkinen, *Chem Commun* **2020**, *56*, 8087–8090.

[29] E. Kalenius, S. Malola, M. F. Matus, R. Kazan, T. Bürgi, H. Häkkinen, *J Am Chem Soc* **2021**, *143*, 1273–1277.

[30] K. Salorinne, S. Malola, O. A. Wong, C. D. Rithner, X. Chen, C. J. Ackerson, H. Häkkinen, *Nat Commun* **2016**, *7*, 10401.

[31] I. Dolamic, B. Varnholt, T. Bürgi, *Nat. Commun.* **2015**, *6*, 7117.

[32] T. G. Schaaff, R. L. Whetten, *J Phys Chem B* **2000**, *104*, 2630–2641.

[33] N. V. Steerteghem, S. V. Cleuvenbergen, S. Deckers, C. Kumara, A. Dass, H. Häkkinen, K. Clays, T. Verbiest, S. Knoppe, *Nanoscale* **2016**, *8*, 12123–12127.